

# Field-Aligned Isotropic Surface Remeshing

Xingyi Du<sup>1,†</sup>, Xiaohan Liu<sup>2,3,†</sup>, Dong-Ming Yan<sup>2,3</sup>, Caigui Jiang<sup>4</sup>, Juntao Ye<sup>2,3</sup>, Hui Zhang<sup>1,\*</sup>

<sup>1</sup>Software School, Tsinghua Univ.

<sup>3</sup>Univ. of Chinese Academy of Sciences

<sup>2</sup>NLPR, Institute of Automation, Chinese Academy of Sciences

<sup>4</sup>Max Planck Institute for Informatics

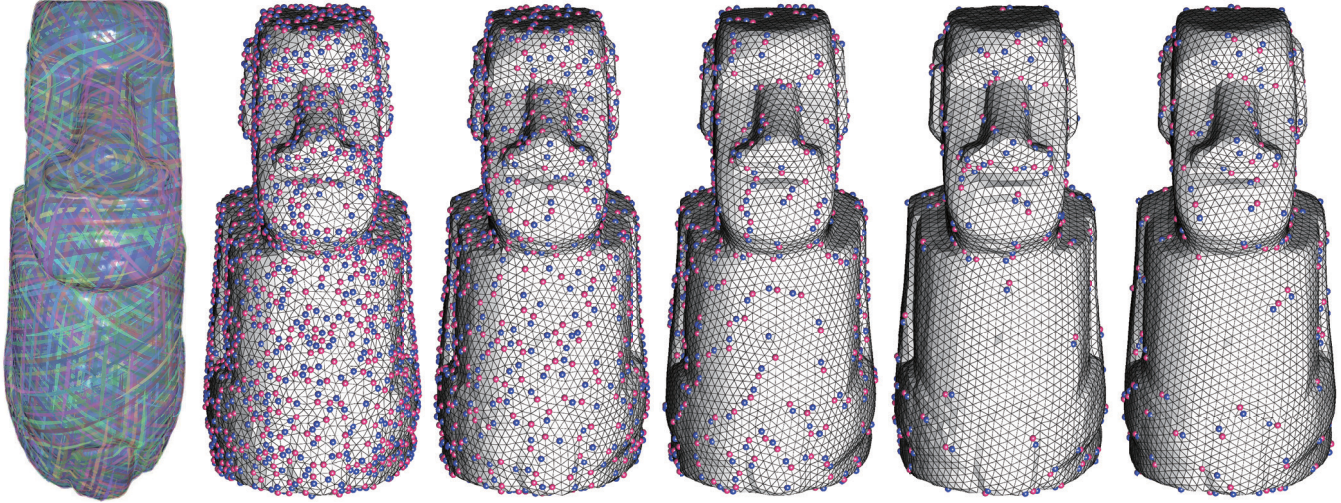


**Figure 1:** Comparison of our approach with representative state-of-the-art approaches; from left to right: 6-RoSy field defining on the Moai surface, remeshing results of blue-noise sampling [YW13], discrete mesh optimization [DVBB13], centroidal Voronoi tessellation [YLL\*09], instant field-aligned meshing [JTPS15], and our result. The irregular vertices of the remeshes are colored blue (degree < 6) and pink (degree > 6). The mesh quality is given in Table 2. Our remeshing is isotropic and field-aligned; i.e., it has a few irregular vertices similar to [JTPS15] while keeping the mesh quality as good as in a CVT-based method [YLL\*09].

## Abstract

We present a novel isotropic surface remeshing algorithm that automatically aligns the mesh edges with an underlying directional field. The alignment is achieved by minimizing an energy function that combines both centroidal Voronoi tessellation (CVT) and the penalty enforced by a six-way rotational symmetry field. The CVT term ensures uniform distribution of the vertices and high remeshing quality, and the field constraint enforces the directional alignment of the edges. Experimental results show that the proposed approach has the advantages of isotropic and field-aligned remeshing. Our algorithm is superior to the representative state-of-the-art approaches in various aspects.

Categories and Subject Descriptors (according to ACM CCS): I.3.6 [Computer Graphics]: Methodology and Techniques—Remeshing

## 1. Introduction

<sup>†</sup> X. Du and X. Liu are joint first authors. \* H. Zhang is the corresponding author.

<sup>2</sup> Triangle meshes are commonly used in computer graphics and other applications. Nowadays, meshes can be acquired with high

accuracy using multiple methods, e.g., using 3D laser scanners, RGBD cameras, dense reconstruction from multi-view stereo images, and isosurface contouring. Using these acquired raw meshes directly in downstream applications is difficult because they usually contain redundant data and have poor mesh quality. Remeshing is necessary to improve mesh quality while preserving the original geometry.

Various application-oriented criteria for surface remeshing are available. In this work, we focus on the widely used isotropic remeshing. Three common criteria should be followed by remeshing algorithms: simplicity, low approximation error, and high mesh quality [AUGA08]. However, these goals usually conflict with one another, e.g., highly regular meshes might have more distorted triangles than irregular meshes, whereas meshes with high triangle quality always contain more singular vertices, e.g., remeshing with *Centroical Voronoi Tessellation* (CVT) [DFG99]. Fig. 1 illustrates this fact.

Directional fields can be naturally defined on surfaces and are commonly used for quadrilateral remeshing. Typical directional fields include principal curvature directions [BLP\*13], conjugate direction fields [LWX\*11], and harmonic fields [DKG05]. The edges of quad meshes are naturally aligned with the underlying fields via global parameterization. However, field alignment in isotropic remeshing is rarely considered. The lack of field-alignment causes "twisting" artifacts near cylindrical regions and surface features, as illustrated in Fig. 4 of [NPPZ11]. Even in isotropic regions, the lack of global alignment leads to local orientation conflict between neighboring areas, and consequently produces unnecessary singular vertices, i.e., possession of valences other than 6, as shown in Fig. 1. The recent work of Jakob et al. [JTPS15] proposed an algorithm called *Instant Field-aligned Meshing* (IFM) for generating isotropic triangle meshes that simultaneously align to a predefined underlying directional field. Although highly regular triangle meshes with only a few singular vertices are generated, triangle quality is sacrificed due to distortion.

In this work, we propose a novel approach for field-aligned isotropic remeshing. We use six-way rotational symmetry (6-RoSy) fields to represent the target orientation of the output mesh edges because 6-RoSy fields are the most natural guidance fields for triangle meshes. However, our formulation can be generalized to other fields. Our method is built upon a remeshing framework that is based on CVT and the *restricted Voronoi diagram* (RVD) on surfaces [YLL\*09]. We add a novel penalty term to the CVT energy function to enforce the mesh edges to align with the underlying field. The presented approach, called FCVT, preserves the advantages of CVT, and the directional features of the field. Furthermore, we incorporate valence optimization operations in our remeshing framework to improve mesh quality. The main contributions of this paper are the following:

- A novel formulation for field-aligned isotropic remeshing.
- A simple interpolation method for 6-RoSy fields.
- A comprehensive comparison of proposed method with recent representative state-of-the-art approaches.

## 2. Related Works

Isotropic surface remeshing has been extensively studied. Representative approaches include particle reactions [Tur92, MKW07, BLW10, AGY\*17], Delaunay insertion [Che93, Boi05, CDS12], discrete local operators [HDD\*93, BK04, AYZ12, DVBB13, HYB\*17], randomized sampling [YW13, GYJZ15, ERA\*16], and variational approaches, e.g., *centroidal Voronoi tessellation* [DFG99], *optimal Delaunay triangulation* (ODT) [Che04], and their variations [FAKG10, CCW12, Ren16]. CVT-based approaches gain considerable attention due to their elegant theoretical background and the capability to generate high-quality meshes. These approaches can further be classified into several categories according to how the Voronoi diagram on surfaces are computed, e.g., mesh parameterization [AMD02, AVDI03, SAG03], discrete clustering [VCP08, LWH\*15], restricted Voronoi diagram [YLL\*09, YBZW14, YW16], and geodesic Voronoi diagram [SSG03, FZ08, WYL\*15, LXY\*16]. Additional details about the recent advantages of surface remeshing are available in the comprehensive survey by Alliez et al. [AUGA08] and the textbook by Botsch et al. [BKP\*10].

Although these isotropic algorithms generate high-quality meshes efficiently, they cannot produce good results near highly non-isotropic regions, e.g., the cylindrical bending areas of CAD models. Anisotropic remeshing algorithms aim to handle such cases, but tend to introduce many thin and long triangles [LB12, ZGW\*13, FLSG14, BSTY15], thereby limiting their use in regular pattern synthesis [NPPZ11], where isotropic elements are preferred.

A natural way to align mesh edges with the principal direction involves defining a directional field on the input domain and then extracting the new mesh from the field with respect to a user-specified precision. The most well-known directional field is the min/max principal curvature directions, which is commonly used for quadrilateral remeshing [BLP\*13] or quad-dominant mixed remeshing [ACSD\*03, LL10].

Isotropic triangle meshes can be extracted from 6-RoSy directional fields through several approaches. For example, Lai et al. [LJX\*10] proposed a method of generating 6-RoSy fields that allow users to fully control and interactively modify the field topology. Huang et al. [HZP\*11] used 6-RoSy and density fields to generate three scalar fields on the input surface and construct meshes by extracting the isolines of the scalar fields. Nieser et al. [NPPZ11] used 6-RoSy field-guided global parameterization to generate triangular and hexagonal meshes. The field is aligned to one of the principal directions, which is automatically selected by the algorithm. However, long and thin triangles produced by parameterization distortion still exist. Jakob et al. [JTPS15] proposed the extrinsic smooth directional field, which aligns better to features than the previous "intrinsic smooth" fields. Nevertheless, the mesh quality of this approach still suffers from distortion caused by tracing the field.

## 3. Field-aligned CVT Formulation

In this work, we propose a novel field-aligned isotropic remeshing algorithm, that is based on CVT and field remeshing techniques. Field alignment is enforced by a penalty term added to the CVT

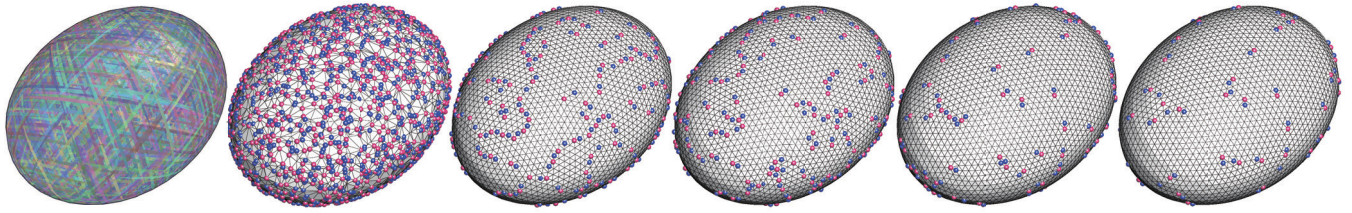


**Figure 2:** From left to right are: the field, initial mesh, result of CVT, result of 10 iterations, 50 iterations and final result.

energy. Given an input mesh surface  $\mathcal{M}$  and a set of sampled points  $\mathbf{X}$  on  $\mathcal{M}$ , we propose the following energy function:

$$E_{tot} = E_{CVT} + \lambda E_{field},$$

where  $\lambda \geq 0$  is a user-specified parameter, which balances the relative importance of the directional alignment requirement. In the rest of this section, we first introduce the basic concepts of CVT, RoSy fields, and the extrinsic smoothness of a given field, and then discuss the details of the proposed field alignment term.

### 3.1. Centroidal Voronoi tessellation

The CVT energy term is defined as

$$E_{CVT}(\mathbf{X}) = \sum_{i=1}^n \int_{\Omega_i|\mathcal{M}} \rho(\mathbf{x}) \|\mathbf{x} - \mathbf{x}_i\|^2 d\sigma, \quad (1)$$

where  $\Omega_i|\mathcal{M}$  is the *restricted Voronoi cell* (RVC) [YLL<sup>\*</sup>09] of the point  $\mathbf{x}_i$  defined as the intersection of the Voronoi cell  $\Omega_i$  of  $\mathbf{x}_i$  and the mesh surface  $\mathcal{M}$ ;  $\rho(\mathbf{x}) > 0$  is a user-defined density function. When  $\rho$  is constant, a uniform CVT is obtained. The dual nature of the RVC as a remeshing of  $\mathcal{M}$  is called *restricted Delaunay triangulation* (RDT).

### 3.2. Rotational symmetry field

The RoSy field is commonly used in parameterization and quadrilateral mesh generation.  $N$ -way rotational symmetry ( $N$ -RoSy) field over a surface defines  $N$  distinct directions at every surface point  $\mathbf{x}$ , where all the directions lie in the tangent plane at  $\mathbf{x}$  and each pair of adjacent directions form an angle of  $\frac{2\pi}{N}$ . Here, a 6-RoSy field is used as the target orientation for mesh edges because it naturally implies the symmetry of regular triangular mesh. Additional details about the directional field are available in recent survey papers [dGDT16, Zha16, VCD<sup>\*</sup>16].

### 3.3. Extrinsic smoothness property

The extrinsic smoothness proposed in [JTPS15] measures the smoothness of a given RoSy field by calculating the difference between proximate field directions directly in 3D space. Jakob et al. [JTPS15] experimentally demonstrated that extrinsic smoothness leads to an improved alignment to the sharp features of the input surface. A theoretical analysis of extrinsic smoothness was also provided by Huang and Ju [HJ16].

Similar to field smoothing, our field alignment solution aims to minimize the difference between the edge direction and the direction of the local field. Inspired by the extrinsic smoothness, we

measure the difference directly in 3D space, thus simply yet powerfully formulating the field alignment constraint.

### 3.4. Field alignment

The field alignment term is formulated as the weighted sum of the directional distance  $D$  of all mesh edges in RDT of  $\mathbf{X}$  on  $\mathcal{M}$ .

$$E_{field}(\mathbf{X}) = \sum_{i=1}^n \sum_{j \in \mathcal{N}(i)} w_{ij} \cdot D_{ij}, \quad (2)$$

where  $\mathcal{N}(i)$  denotes the neighbor points of  $\mathbf{x}_i$  and  $w_{ij}$  is the weight of edge  $e_{ij}$ .

A detailed derivation of the direction distance  $D$  is provided, and its properties in the case of 6-RoSy field is discussed. Given a sample point  $\mathbf{x}_i$  and its neighbor point  $\mathbf{x}_j$ ,  $e_{ij} = \mathbf{x}_j - \mathbf{x}_i$  is the direction vector of the edge between  $\mathbf{x}_i$  and  $\mathbf{x}_j$ ,  $n_i$  is the unit normal vector and  $d_i$  is the unit vector representing the  $N$ -RoSy field, i.e. one of the  $N$  field vectors at  $\mathbf{x}_i$ .

Given  $n_i$  and  $d_i$ , a local coordinate system is established by a tuple of standard unit vectors  $\{d_i, n_i \times d_i, n_i\}$ . The directional angles  $\theta$  and  $\varphi$  of edge  $e_{ij}$  is then defined through a method common in spherical systems, as shown in Fig. 3 (middle). The direction similarity of edge  $e_{ij}$  and local field  $d_i$  can simply be measured by their inner product:

$$\begin{aligned} d_i^T \left( \frac{e_{ij}}{\|e_{ij}\|} \right) &= (1, 0, 0) \cdot (\sin \theta \cos \varphi, \sin \theta \sin \varphi, \cos \theta)^T \\ &= \sin \theta \cos \varphi. \end{aligned}$$

To accord with the symmetry of the  $N$ -RoSy field,  $\varphi$  is multiplied with the symmetry number  $N$ , thereby giving the  $N$ -RoSy direction similarity  $S$ ,

$$S(e_{ij}, n_i, d_i) = \sin \theta \cos(N\varphi).$$

$S$  is a  $\frac{2\pi}{N}$  period function of  $\varphi$  and thus not affected by the choice of  $d_i$ . To obtain the  $N$ -RoSy direction distance, we first map  $\cos(N\varphi)$  linearly to  $[0, 1]$ , which simultaneously maps  $S$  to  $[0, 1]$ . Then, we calculate the difference between 1 and the image of  $S$ . The  $N$ -RoSy direction distance  $D$  is

$$D(e_{ij}, n_i, d_i) = 1 - \left( \frac{1 + \cos(N\varphi)}{2} \right) \sin \theta, \quad D \in [0, 1]. \quad (3)$$

To obtain an intuition of the field alignment term, we explore the 6-RoSy direction distance,

$$D_6 = 1 - \left( \frac{1 + \cos 6\varphi}{2} \right) \sin \theta.$$

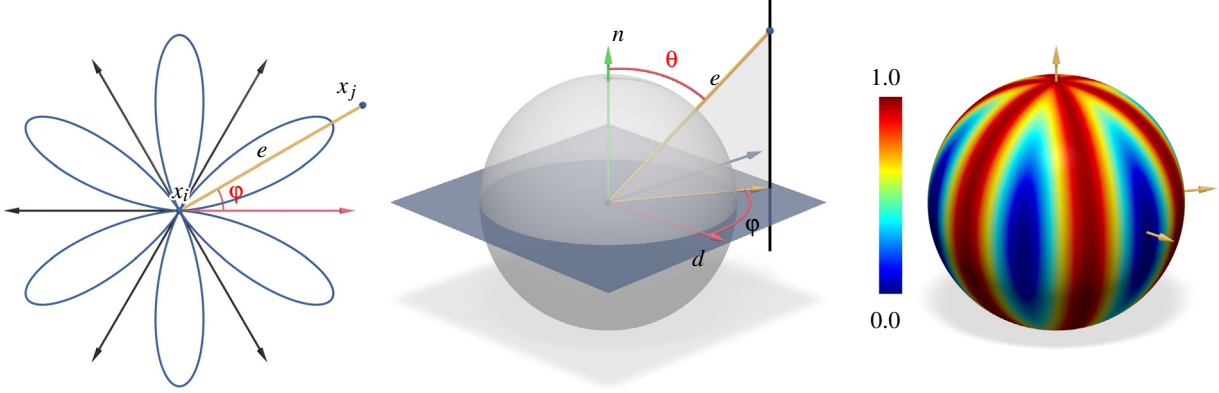


**Figure 3:** Left: 6-RoSy direction distance in 2D plane; middle: Local coordinate system formed with local unit normal  $n$  and the representing field vector  $d$  at sample point; direction angles of edge  $e$  defined in local coordinate system; right: visualized 6-RoSy direction distance  $D_6$  on unit sphere; distance penalizes deviation from local field and restricts edges on the tangent plane.

Fig. 3 (right) visualizes  $D_6$  on the surface of a unit sphere. Direction distance penalizes deviation from the local field and correctly represents the rotational symmetry. Fig. 3 (left) illustrates  $D_6$  on the equatorial plane ( $\theta = \frac{\pi}{2}$ ). The direction distance is 0 when the edge coincides with one of the field directions and increases when the edge deviates from the field. Furthermore, distance restricts mesh edges to be on the local tangent plane because  $D_6$  will increase if  $\theta$  deviates from  $\frac{\pi}{2}$ .

#### 4. Implementation Details

In this section, we present the implementation details of our field-aligned isotropic remeshing framework. The main building blocks are field initialization, interpolation, and energy minimization.

##### 4.1. Direction field initialization

We use the direction field generation proposed in [JTPS15], which uses a mesh  $\mathcal{M}$  as input and outputs the normal and field directions for each vertex of  $\mathcal{M}$ . Normal and field directions are represented by unit 3D vectors. For triangle remeshing, a 6-RoSy field is used.

##### 4.2. Direction field interpolation

To calculate the field alignment energy term for each sample point, the normal and field directions at the point are required. However, the generated field is only defined on the vertices of the input mesh. Thus, the field direction over the entire mesh surface must be interpolated.

Direction interpolation over surface is a hard problem, especially for an  $N$ -RoSy field. For a 6-RoSy field, any of the six direction vectors can be chosen to represent the field direction at each vertex. Therefore, the interpolation method requires that the output direction is not affected by the choice of field representation. Besides, a smooth interpolation is desired to facilitate energy optimization, and this interpolation is not addressed in [JTPS15].

Here, we propose a novel interpolation scheme that interpolates normal and field directions over the mesh surface. We follow the piecewise paradigm to allow the interpolation result in a mesh triangle to be determined by the direction information at its three vertices.

Fig. 5 shows the interpolation at point  $X$  in  $\triangle ABC$ . First, the normal direction is calculated as a weighted average of the normal directions of the three vertices:

$$n = w_A n_A + w_B n_B + w_C n_C.$$

Here, we use the well-known discrete harmonic weights, as suggested in [HJ16]. Then, we normalize the normal direction to unit

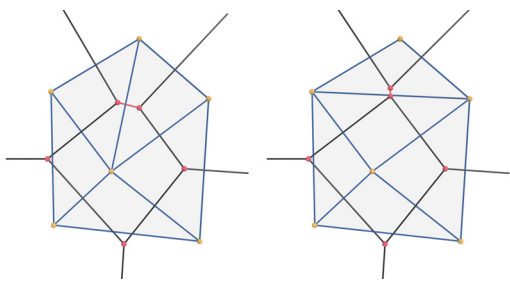


**Figure 4:** Delaunay triangulation and its dual Voronoi diagram when an edge flips.

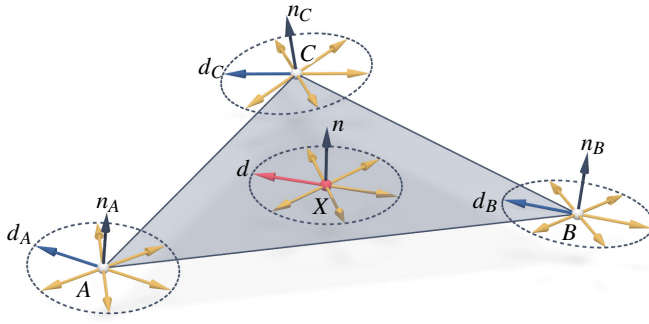


**Figure 5:** Normal and field direction interpolation in  $\triangle ABC$ .

length. Given the normal direction  $n$ , the field direction is restricted to be orthogonal to  $n$ . The direction  $d$  that has the least angle deviation from the field directions at the three vertices is then found. Formally,  $d$  is determined as the maximizer of the following energy:

$$\begin{aligned} E_{\text{interpolation}} &= w_A d_A^T d + w_B d_B^T d + w_C d_C^T d \\ &= (w_A d_A + w_B d_B + w_C d_C)^T d \\ &= d_w^T d, \end{aligned}$$

where  $d_w$  denotes the weighted average of the field directions, which can be decomposed into two components: one orthogonal another parallel to the normal vector  $n$ :

$$d_w = nn^T d_w + (I - nn^T) d_w.$$

Thus, the energy becomes

$$\begin{aligned} E_{\text{interpolation}} &= d_w^T d \\ &= d_w^T nn^T d + d_w^T (I - nn^T) d \\ &= d_w^T (I - nn^T) d. \end{aligned}$$

The energy is maximized when  $d$  has the same direction as  $(I - nn^T) d_w$ , and the maximal energy is  $\|(I - nn^T) d_w\|$ . To eliminate the influence of the choice of representative vectors at the three vertices, we traverse all combinations of these vectors to find the combination that maximizes  $\|(I - nn^T) d_w\|$ , thus also optimizing energy  $E_{\text{interpolation}}$ . Meanwhile, interpolated field direction  $d$  is set to be length-normalized  $(I - nn^T) d_w$ , which is produced by this combination of representation vectors.

Our method shares the concept of extrinsic field smoothness used in [HJ16] such that the difference between two directions is measured directly in 3D space. The result of interpolation is not affected by the choice of representative vectors. With a proper choice of weight, the smoothness is also guaranteed. Our interpolation method is simple and can be generalized to any arbitrary  $N$ -RoSy field.

### 4.3. Energy minimization

We use a quasi-Newton solver (e.g., L-BFGS [LWL\*09]) to minimize the proposed energy function, where the functional gradient with respect to points  $\mathbf{X}$  is required. The gradient is composed of two parts  $E_{CVT}$  and  $E_{field}$ .

$$\frac{\partial E_{tot}}{\partial \mathbf{X}} = \frac{\partial E_{CVT}}{\partial \mathbf{X}} + \lambda \frac{\partial E_{field}}{\partial \mathbf{X}}.$$

Here,  $\frac{\partial E_{CVT}}{\partial \mathbf{x}_i} = 2m_i(\mathbf{x}_i - \mathbf{x}_i^*)$  [DFG99], where  $m_i$  is the mass of the RVC  $\Omega_{i|\mathcal{M}}$  and  $\mathbf{x}_i^*$  is the restricted centroid [YLL\*09].

For  $E_{field}$ , the partial derivative with respect to a sample point  $\mathbf{x}_i$  is

$$\frac{\partial E_{field}}{\partial \mathbf{x}_i} = \sum_{j \in \mathcal{N}(i)} \left( w_{ij} \cdot \frac{\partial D_{ij}}{\partial \mathbf{x}_i} + w_{ji} \cdot \frac{\partial D_{ji}}{\partial \mathbf{x}_i} \right),$$

where  $\mathcal{N}(i)$  denotes the neighbors of  $\mathbf{x}_i$ ,  $w_{ij}$  and  $w_{ji}$  are edge weights, and  $D$  is the direction distance function. The detailed calculation of the gradient of  $D$  is given in the Appendix.

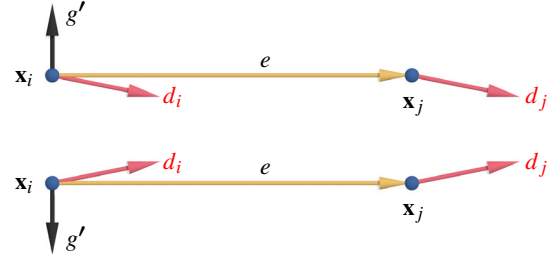


**Figure 6:** Opposite gradient directions of field alignment energy in two different constant fields.

To demonstrate the effectiveness of our field alignment term, we analyze the energy gradient through a simple case of a 6-RoSy field in 2D plane, where  $\theta$  is always  $\pi/2$ . In the following discussion, we assume a Cartesian coordinate system with standard unit vectors  $\{e_x, e_y, e_z\}$ , in which  $e_x$  and  $e_y$  lie in the 2D plane, and  $e_z$  is the normal direction. The partial derivative of the field alignment term of edge  $e$  with respect to  $\mathbf{x}_i$  is

$$\frac{\partial E_e}{\partial \mathbf{x}_i} = 3(\sin 6(\varphi_e - \delta_i) + \sin 6(\varphi_e - \delta_j)) \cdot \frac{e \times e_z}{\|e\|^2},$$

where  $\varphi_e$  is the directional angle of edge  $e$ ;  $\delta_i$  and  $\delta_j$  are the angles of field direction at  $\mathbf{x}_i$  and  $\mathbf{x}_j$ , respectively. These angles are relative to  $e_x$ .

Fig. 6 shows an edge in two different constant fields. In both cases, the opposite gradient direction  $g'$  is the right moving direction for  $\mathbf{x}_i$  to align the edge with the field.

### 4.4. Valence optimization

After energy optimization, we optimize vertex valence by minimizing the following mesh irregularity energy function:

$$R = \sum_{v \in V} (d(v) - o(v))^2,$$

where  $d(v)$  is the valence of  $v$  and  $o(v)$  is the optimal valence of  $v$ , which is usually set as 6 for inner vertices and 4 for boundary vertices.

Similar to previous approaches [BK04, DVBB13], we use three topology operators, i.e., edge flip, edge collapse, and vertex split, to minimize the energy function. For each irregular vertex, we find the topology operation that decreases the irregularity energy the most. In each iteration, operations that decrease the irregularity the most

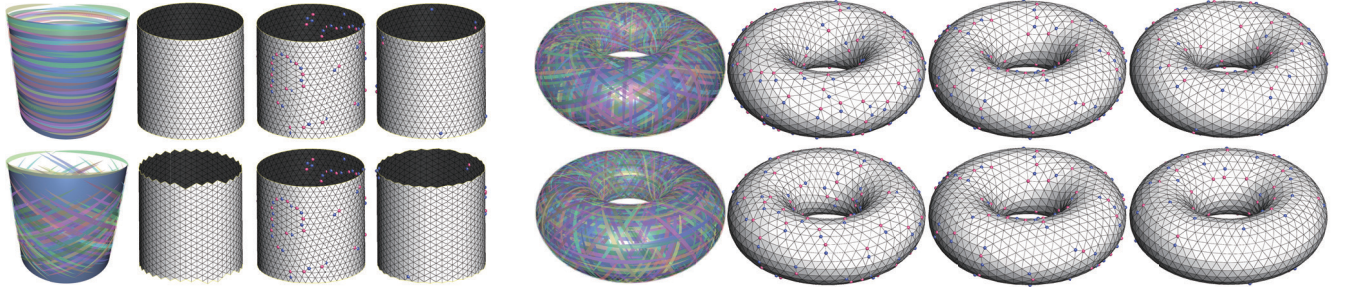


**Figure 7:** Applying proposed approach on cylinder and torus models, whose maximal (top) and minimal (bottom) curvature directions are used as vector field; from left to right of each example: vector fields, and results of IFM, CVT, and proposed method.

are selected and applied. After each topology operation, local tangential smoothing is applied to repair the distortion induced by the operation. After valence optimization, several FCVT iterations are performed to re-align mesh edges from possible deviation caused by valence optimization.

## 5. Experimental Results

The typical pipeline of our remeshing algorithm includes vector field generation, random initial sampling, CVT optimization, and FCVT optimization, as illustrated in Fig. 2. We use the open-source library Geogram [geo] for CVT computation and the program Instant Meshes program [JTPS15] for vector field generation. All examples shown in this paper are produced on a PC with 4.00 Ghz CPU, 16 GB RAM, and Win10 operating system. To eliminate the influence of the size of input models and the number of target sample points, we set the scale of each input models, thus making the average area per sample point constant. The optimization process is terminated when the  $L_2$  norm of the energy gradient divided by the number of sample points is less than  $10^{-5}$ . The performance and the convergence behavior of our algorithm are analyzed. Then, a detailed analysis of each parameter involved in our method is provided. Finally, we evaluate and compare our results with those of representative state-of-the-art remeshing techniques.

**Convergence and performance.** First, we verify the effectiveness of our algorithm on two specific input models, i.e., a cylinder and a torus, whose vector fields are manually chosen to be one of the principal curvature directions. As shown in Fig. 7, our method can capture the field information accurately, even for special inputs. Our results contain very few singular vertices, which cannot be eliminated due to the global nature of mesh connectivity. We compare our results with those of IFM. For the cylinder model, IFM can generate singular-free results because of the open-boundary condition, whereas ours contain a few singularities that can be simply removed by pushing them to the boundary using the singularity move operation proposed in [LZKW10]. For the torus model, our method provides better results with fewer singularities. In both tests, our method exhibits a field alignment property similar to that of IFM and preserves the advantage of good mesh quality of the CVT method (Table 2).

Next, we analyze the convergence behavior of the proposed energy function. We apply our algorithm to three representative models and observe the convergence behavior of the CVT energy

and field-aligned energy. We track the average energy per sample point during the process. The pure CVT optimization is first applied to acquire a uniform sample distribution. Then, the field alignment term is enforced to improve edge orientation. Fig. 8 shows our experimental result. The Torus model has approximately 4k faces and 1k sample points, whereas the Botijo and Bunny models have approximately 80k faces and 3k sample points. Standard CVT and FCVT optimization both converge in approximately 100 iterations. Moreover, the resulting average energy per sample point is nearly constant regardless of input model and number of sample points. These findings verify the stability of our method against various inputs.

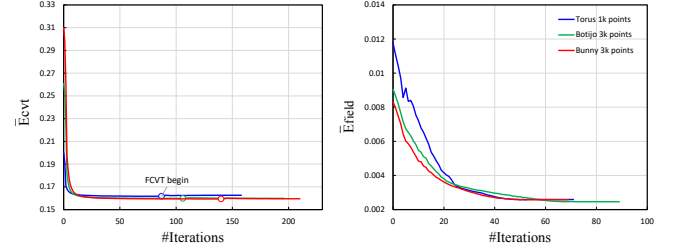


**Figure 8:** Energy analysis; FCVT is performed after pure CVT convergence for three models: Torus(4k faces), Botijo(82k faces) and Bunny(72k faces); FCVT optimization also keeps CVT energy at low level.

Our approach is based on energy minimization; thus, the performance is not as efficient as that of IFM, which is based on vector field tracing. Our algorithm performs slightly poorer in comparison with the standard CVT algorithm [YLL\*09] due to the additional gradient and energy evaluation of the field alignment term. However, the most time-consuming part of the CVT framework is the RVD computation, which has a parallel version of the implementation on multi-core CPUs [geo]; therefore, our algorithm is fast and comparable to other approaches running on a multi-core CPU.

**Uneven initial sampling.** Points are uniformly sampled over the input surface with respect to the density function for initialization. However, our method is also capable of handling uneven initialization. We first run Lloyd iteration several times to achieve improved initialization, and then switch to the optimization process described in Sec. 3. We test CVT and our method on a cylinder model with random and uneven initial sampling. Fig. 9 shows the results. CVT and our method can properly handle uneven initial sampling.

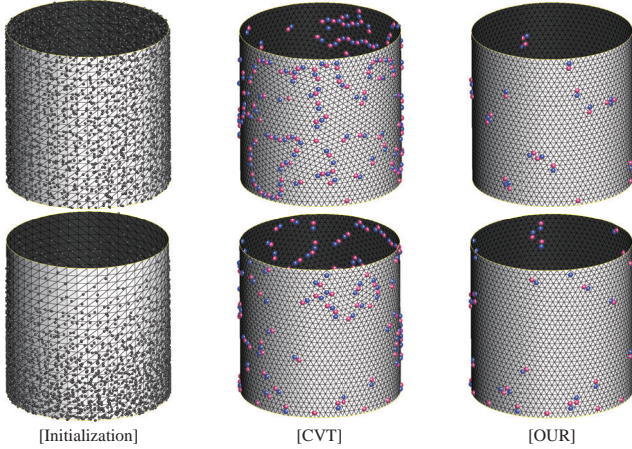


**Figure 9:** Influence of uneven initial sampling.

**Influence of  $\lambda$ .** All the input models are scaled such that the average area per RVC is constant to normalize the parameter  $\lambda$ . We test various choices of  $\lambda$  for different models and resolutions. The overall observation is that a smaller  $\lambda$  results in better triangle quality but more singular vertices and a larger  $\lambda$  reduces the number of singular points but sacrifices mesh quality. Fig. 10 shows the influence on valence and average triangle quality of varying  $\lambda$  on different models. For all the experiments, we use a constant  $\lambda$  of 0.0075.

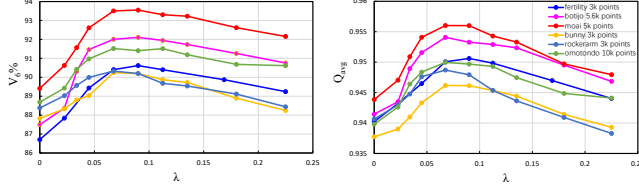


**Figure 10:** Influence of  $\lambda$ .

**Valence optimization.** To validate the effectiveness of valence optimization, we compare remeshing results with and without valence optimization on the Botijo model. Three methods (CVT, FCVT, and IFM) are used to remesh the model. Table 1 shows the result. For all methods, the rate of regular vertex increases after valence optimization, thereby affirming the effectiveness of our valence optimization. By contrast, other metrics, such as average quality, are relatively insensitive probable because the regular area already occupies a major part of the mesh before valence optimization, thus making the improvement by valence optimization less remarkable. The experiments also show that FCVT is superior to CVT in average quality and regular rate even without valence optimization.

**Influence of resolution.** We also test the performance of our algorithm under different target mesh resolutions, i.e., different numbers of sample points. The experiment is conducted on a torus model with 1.8k vertices. For various target resolutions, we perform CVT, FCVT, and IFM and compare the quality of the output meshes. To clarify the comparison, we only focus on the energy minimization stage, and omit valence optimization. For each resolution, the experiment is repeated five times. Fig. 11 illustrates the results.

method	$Q_{avg}$	$\theta_{min}$	$V_6\%$
CVT	0.94	40.3	86.9
CVT_Valence	0.94	39.4	90.7
OUR	0.95	37.8	92.4
OUR_Valence	0.95	37.5	93.7
IFM	0.96	17.7	93.0
IFM_Valence	0.96	19.8	94.5

**Table 1:** Influence of valence optimization.

We measure two groups of mesh qualities, i.e., average and extreme qualities. The average qualities include the average triangle quality  $Q_{avg}$ , average minimal angle  $\theta_{min}$ , and percentage of valence-6 vertices  $V_6\%$ , which represent mesh quality in an average sense. Extreme qualities, such as  $Q_{min}$ ,  $\theta_{min}$ , and  $\theta_{max}$  focus on extreme values and quality bound. In our experiments, the average qualities generally benefit from field alignment, and this effect is further enhanced by increasing the output resolution, as can be seen from the first column of Fig. 11. By contrast, extreme qualities are not significantly affected by resolution and deteriorate only slightly with increasing resolution, as illustrated by the second column of Fig. 11. Meanwhile, CVT has an evident advantage over IFM in these extreme qualities, which is also preserved by FCVT.

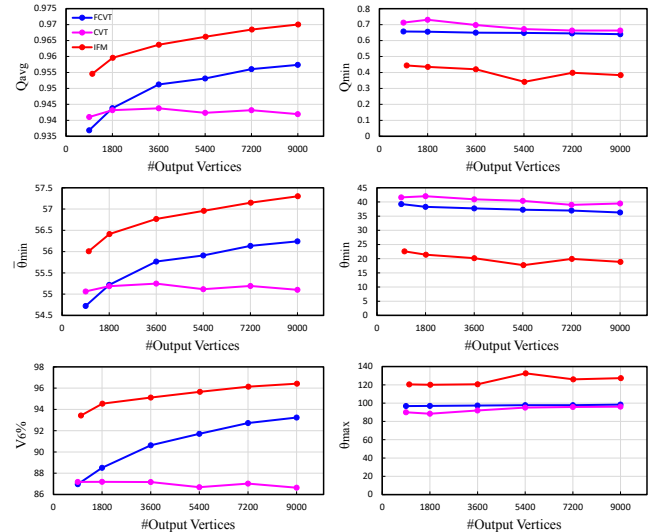


**Figure 11:** Influence of output resolution on mesh quality. The experiment is performed on a torus model with 1.8k vertices. The left column shows FCVT and IFM have improved mesh qualities with denser output resolution. The right column shows that FCVT has preserved the advantage of CVT over IFM on some mesh qualities.

For extreme mesh qualities, FCVT inherits the advantage of CVT. In addition, the field alignment capability of FCVT enables improvement of average qualities and a similar positive response to output resolution, such as IFM. Another interesting observation is that the critical resolution where FCVT outperforms CVT in average qualities is approximately 1.8k, i.e., the resolution of the input model. This finding is related to the piecewise harmonic field interpolation scheme used by FCVT. The piecewise harmonic in-

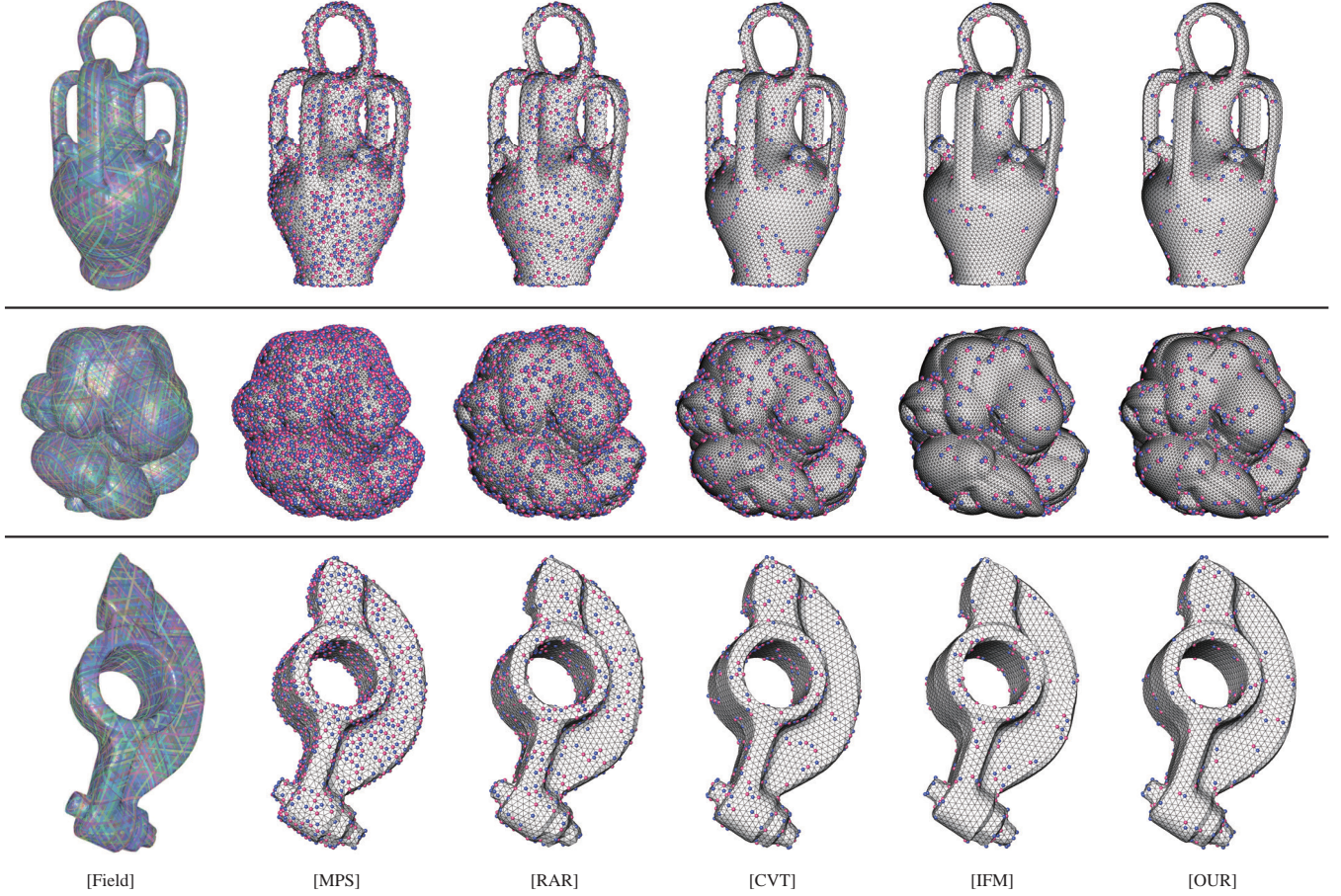


**Figure 12:** Comparison of uniform sampling results; from top to bottom: results of Botijo, Bunny, Omotondo and Rockerarm; from left to right: visualized direction fields and remeshing results of MPS [YW13], RAR [DVBB13], CVT [YLL\*09], IFM [JTPS15] and FCVT; quality comparison given in Table 2.

terpolation may lead to a smoother field in the interior of a triangle than at the common edge of two adjacent triangles. With increasing resolution, more pairs of adjacent sample points share the same input triangle rather than reside on different triangles, thus improving overall energy smoothness and improving mesh quality. The results in the left column of Fig. 11 also validate the effectiveness of our field interpolation algorithm. According to [JTPS15], IFM requires the input mesh to have higher resolution than the output; otherwise, the input mesh has to be further subdivided. These results imply that our interpolated field is comparable with the field produced by the “subdivide and optimize” process of IFM.

**Sharp feature handling.** Our method is also able to handle input meshes with sharp features. The features on the input mesh are either detected automatically by certain algorithms or manually selected by the user. Similar to [YLL\*09], a two-stage strategy is used to preserve sharp features. In the first stage, sample points are optimized freely to obtain an optimal distribution. In the second stage, each sample point whose RVC intersects with a feature line is snapped onto the line and confined on the feature in the following optimization. Fig. 14 shows several results of our method applied to models with sharp features.

**Comparison.** We first compare our approach with the most related approaches, i.e., CVT and IFM, in terms of visual effect and mesh quality. Our results are obtained by first applying 65 CVT iterations and then 65 FCVT iterations. The results of CVT are obtained by applying 130 CVT iterations (or less if converged earlier). The visual effect (Fig. 1, 7, 12, and 13) shows that our results are well aligned to the underlying vector fields, which are able to capture the anisotropic features as well as produce well-shaped triangle. Moreover, the singular point distribution of our approach is similar to that of IFM.

We compare our method with IFM [JTPS15] on adaptive remeshing in Fig. 13. Adapting the edge length locally is difficult due to the global nature of IFM, thereby resulting in a large distortion in regions with highly changing density. Fig. 15 shows another example that uses a density function with large gradation.

Our results are compared with several representative state-of-the-art approaches, including *maximal Poisson-disk sampling* (MPS) [YW13], *realtime adaptive remeshing* (RAR) based on local connectivity optimization [DVBB13]. We use the standard mesh quality evaluation metric for comparison. The quality of a triangle

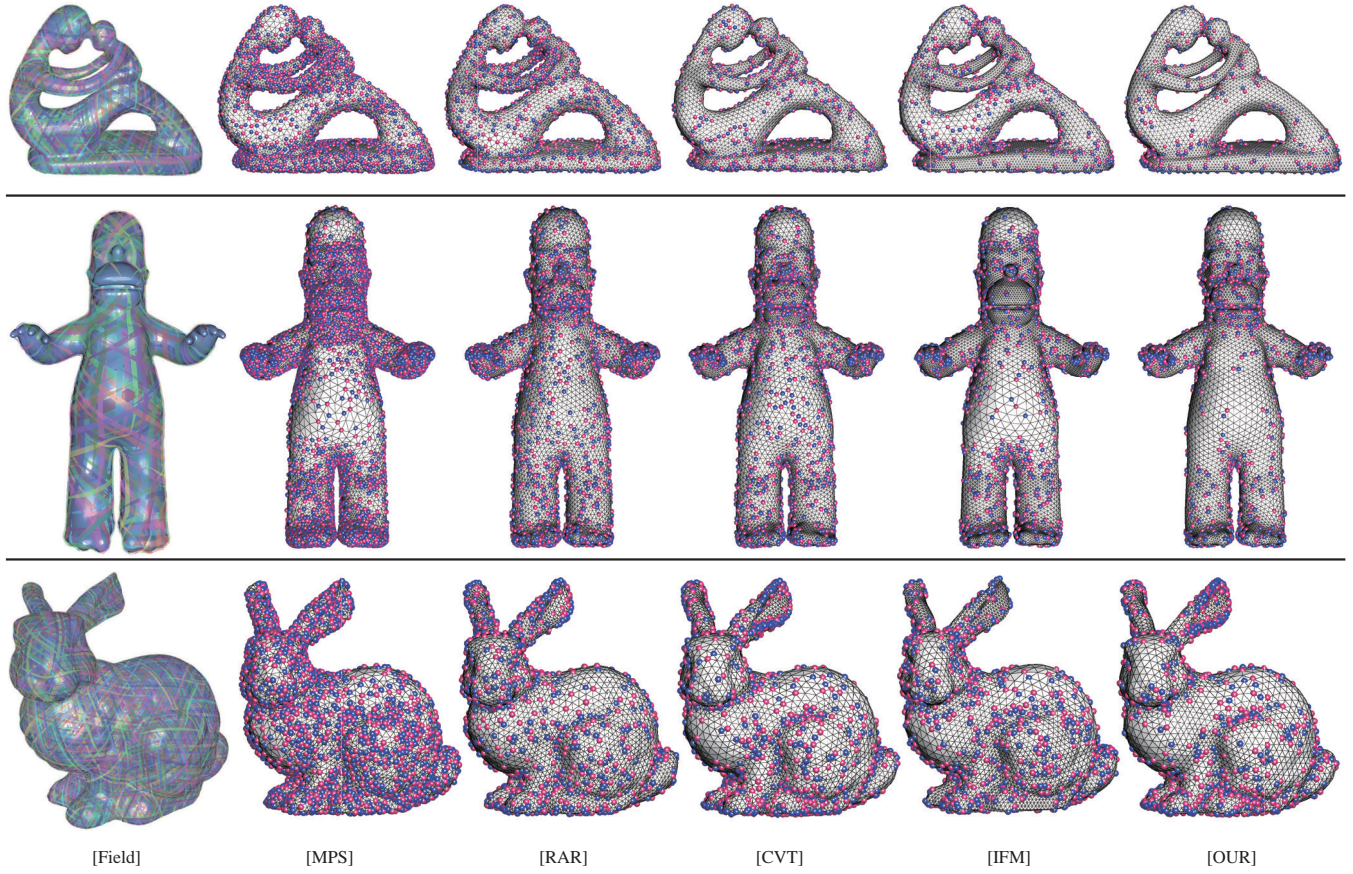


**Figure 13:** Comparison of adaptive sampling results; From left to right: visualized of direction fields, remeshing results of MPS [YW13], RAR [DVBB13], CVT [YLL\*09], IFM [JTPS15] and ours. The quality comparison given in Table 2.

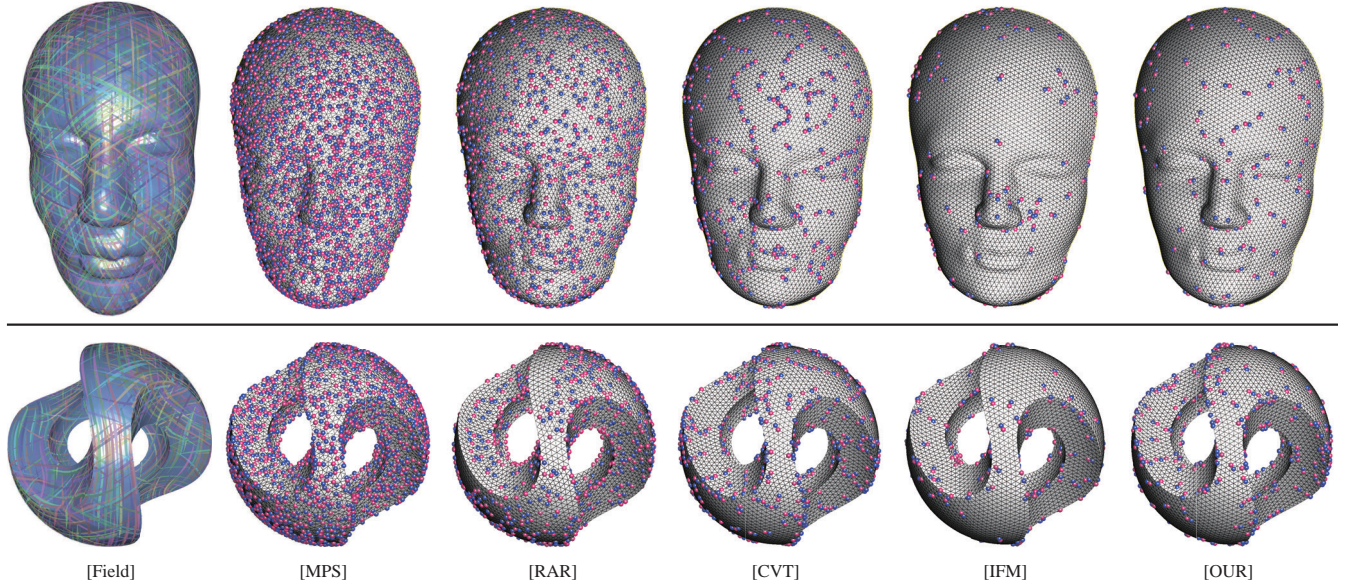


**Figure 14:** Results of feature preservation.

is measured by  $Q(t) = \frac{2\sqrt{3}|t|}{p_t h_t}$ , where  $|t|$  is the area of triangle  $t$ ,  $p_t$  the inscribed radius of  $t$  and  $h_t$  the length of the longest edge of  $t$ . An equilateral triangle has  $Q(t) = 1$  and a degenerate triangle has  $Q(t) = 0$  [FB97]. Table 2 lists the numerical statistics of all the compared approaches. In addition to the quality measured in Fig. 11, we count the percentage of the triangles with small and large angles, e.g.,  $\theta_{min} < 30^\circ$  and  $\theta_{max} > 90^\circ$ , which reflect the overall triangle quality distribution of each method. Finally, we measure the Hausdorff distance and the root mean square error between the remesh and the input mesh. From quantitative comparison, our approach preserves the advantages of isotropic and field remeshing. For most models in the experiments, our results have better  $\theta_{min}$  than IFM, and better regularity than MPS, RAR, and CVT.

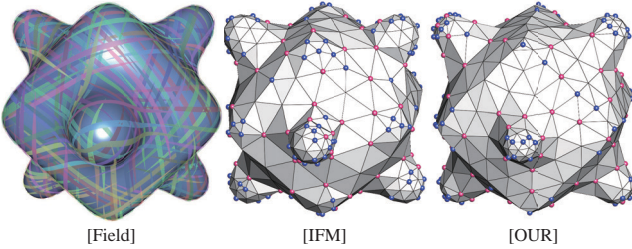


**Figure 15:** Comparison of adaptive remeshing with IFM. Both IFM and our method are able to generate meshes with large triangle area contrast. However, our result better aligns to the underlying shape and is less distorted compared to the result of IFM.

**Limitation.** Our current approach has certain limitations. First, in the adaptive sampling scenario, the remeshing result is not as good as that of CVT, because the density function always conflicts with the field alignment constraint. Another limitation is that the field interpolation is somehow time-consuming: in this process, we have to project each sample back onto the surface and transverse all combinations of representative vectors. We plan to address upon these problems in our future work.

## 6. Conclusion and Future Work

We present a novel approach that combines the CVT-based isotropic remeshing with vector field alignment. Unlike approaches that modify the distance metrics [LL10, SCW<sup>\*</sup>11], we impose the field alignment as a penalty term added to the standard CVT energy function, thus simplifying implementation. Our results exhibit the advantages of isotropic and field-aligned remeshing, i.e., few singularities and high mesh quality. In the future, we plan to use the field defined on facets instead of vertices, which may improve performance. Another interesting problem is finding the correspondence between singularities of the input field and resulting mesh, which may help to detect and eliminate unnecessary singular vertices. Reducing the shape approximation error is also of considerable interest. We would also like to further exploit the power of our approach in potential applications.

## Acknowledgements

We are grateful to anonymous reviewers for their suggestive comments. We would like to thank Wenzel Jacob and Daniele Panozzo for sharing the source code of the adaptive version of IFM [JTPS15] for comparison. This work is partially funded by the National Natural Science Foundation of China (61373070, 61772523, 61372168, 61379096, 61620106003).

## References

- [ACSD<sup>\*</sup>03] ALLIEZ P., COHEN-STEINER D., DEVILLERS O., LÉVY B., DESBRUN M.: Anisotropic polygonal remeshing. *ACM Trans. on Graphics (Proc. SIGGRAPH)* 22, 3 (2003), 485–493. [2](#)
- [AGY<sup>\*</sup>17] AHMED A., GUO J., YAN D.-M., FRANCESCHI J.-Y., ZHANG X., DEUSSEN O.: A simple push-pull algorithm for blue-noise sampling. *IEEE Trans. on Vis. and Comp. Graphics* 23, 12 (2017), 2496–2508. [2](#)
- [AMD02] ALLIEZ P., MEYER M., DESBRUN M.: Interactive Geometry Remeshing. *ACM Trans. on Graphics (Proc. SIGGRAPH)* 21(3) (2002), 347–354. [2](#)
- [AUGA08] ALLIEZ P., UCELLI G., GOTSMAN C., ATTENE M.: Recent advances in remeshing of surfaces. In *Shape Analysis and Structuring* (2008), pp. 53–82. [2](#)
- [AVDI03] ALLIEZ P., VERDIÉRE É. C. d., DEVILLERS O., ISENBURG M.: Isotropic surface remeshing. In *Shape Modeling International - SMI* (2003), pp. 49–58. [2](#)
- [AYZ12] AGHDAAI N., YOUNES H., ZHANG H.: 5–6–7 meshes: Remeshing and analysis. *Computers & Graphics* 36, 8 (2012), 1072–1083. [2](#)
- [BK04] BOTSCHE M., KOBBELT L.: A remeshing approach to multiresolution modeling. In *Proc. of Symp. of Geometry Processing* (2004), pp. 189–196. [2, 5](#)
- [BKP<sup>\*</sup>10] BOTSCHE M., KOBBELT L., PAULY M., ALLIEZ P., LÉVY B.: *Polygon Mesh Processing*. AK Peters, 2010. [2](#)
- [BLP<sup>\*</sup>13] BOMMES D., LÉVY B., PIETRONI N., PUPPO E., SILVA C. T., TARINI M., ZORIN D.: Quad-mesh generation and processing: A survey. *Computer Graphics Forum* 32, 6 (2013), 51–76. [2](#)
- [BLW10] BRONSON J. R., LEVINE J. A., WHITAKER R. T.: Particle systems for adaptive, isotropic meshing of CAD models. In *Proc. of the 19th International Meshing Roundtable* (2010), Shontz S., (Ed.), pp. 279–296. [2](#)
- [Boi05] BOISSONNAT J.-D. O. S.: Provably good sampling and meshing of surfaces. *Graphical Models* 67 (2005), 405–451. [2](#)
- [BSTY15] BOISSONNAT J., SHI K., TOURNOIS J., YVINEC M.: Anisotropic Delaunay meshes of surfaces. *ACM Trans. on Graphics* 34, 2 (2015), 14:1–14:11. [2](#)
- [CCW12] CHEN Z., CAO J., WANG W.: Isotropic surface remeshing using constrained centroidal Delaunay mesh. *Computer Graphics Forum* 31, 7-1 (2012), 2077–2085. [2](#)
- [CDS12] CHENG S.-W., DEY T. K., SHEWCHUK J. R.: *Delaunay Mesh Generation*. CRC Press, 2012. [2](#)
- [Che93] CHEW L. P.: Guaranteed-quality mesh generation for curved surfaces. In *Proceedings of the Ninth Symposium on Computational Geometry* (1993), pp. 274–280. [2](#)
- [Che04] CHEN L.: Mesh smoothing schemes based on optimal Delaunay triangulations. p. 109ÍC120. [2](#)
- [DFG99] DU Q., FABER V., GUNZBURGER M.: Centroidal Voronoi tessellations: applications and algorithms. *SIAM Review* 41 (1999), 637–676. [2, 5](#)
- [dGDT16] DE GOES F., DESBRUN M., TONG Y.: Vector field processing on triangle meshes. In *ACM SIGGRAPH 2016 Courses* (2016), SIGGRAPH ’16, pp. 27:1–27:49. [3](#)



- 504 [DKG05] DONG S., KIRCHER S., GARLAND M.: Harmonic functions 565  
 505 for quadrilateral remeshing of arbitrary manifolds. *Comp. Aided Geom.* 566  
 506 *Design* 22, 5 (2005), 392 – 423. 2
- 507 [DVBB13] DUNYACH M., VANDERHAEGHE D., BARTHE L., BOTSCHE 569  
 508 M.: Adaptive remeshing for real-time mesh deformation. In *Euro-* 570  
*509 graphics Short Papers Proceedings* (2013), pp. 29–32. 1, 2, 5, 8, 9
- 510 [ERA\*16] EBEIDA M., RUSHDI A. A., AWAD M. A., MAHMOUD 572  
 511 A. H., YAN D.-M., ENGLISH S. A., OWENS J. D., BAJAJ C. L., MIT- 573  
 512 CHELL S. A.: Disk density tuning of a maximal random packing. *Com-* 574  
*513 puter Graphics Forum (Proc. SGP)* 35, 5 (2016), 259–269. 2
- 514 [FAKG10] FUHRMANN S., ACKERMANN J., KALBE T., GOESELE M.: 575  
 515 Direct resampling for isotropic surface remeshing. In *Proceedings of the* 576  
*516 Vision, Modeling, and Visualization Workshop 2010* (2010), pp. 9–16. 2
- 517 [FB97] FREY P. J., BOROUCHAKI H.: Surface mesh evaluation. In *IMR* 578  
 518 (1997), pp. 363–374. 10
- 519 [FLSG14] FU X., LIU Y., SNYDER J., GUO B.: Anisotropic simplicial 580  
 520 meshing using local convex functions. *ACM Trans. on Graphics (Proc.* 581  
*SIGGRAPH Asia*) 33, 6 (2014), 182:1–182:11. 2
- 522 [FZ08] FU Y., ZHOU B.: Direct sampling on surfaces for high quality 583  
 523 remeshing. In *ACM symposium on Solid and physical modeling* (2008), 584  
 524 pp. 115–124. 2
- 525 [geo] GEOGRAM. <https://gforge.inria.fr/projects/geogram/>. 6
- 526 [GYJZ15] GUO J., YAN D.-M., JIA X., ZHANG X.: Efficient maxi- 586  
 527 mal Poisson-disk sampling and remeshing on surfaces. *Computers &* 587  
*528 Graphics* 46, 6-8 (2015), 72–79. 2
- 529 [HDD\*93] HOPPE H., DEROSE T., DUCHAMP T., McDONALD J., 591  
 530 STUETZLE W.: Mesh optimization. In *Proc. ACM SIGGRAPH* (1993), 592  
 531 pp. 19–26. 2
- 532 [HJ16] HUANG Z., JU T.: Extrinsicly smooth direction fields. *Compu-* 593  
*533 ters & Graphics* 58 (2016), 109–117. 3, 4, 5
- 534 [HYB\*17] HU K., YAN D.-M., BOMMES D., ALLIEZ P., BENES B.: 596  
 535 Error-bounded and feature preserving surface remeshing with minimal 597  
 536 angle improvement. *IEEE Trans. on Vis. and Comp. Graphics* 23, 12 598  
 (2017), 2560–2573. 2
- 538 [HZP\*11] HUANG J., ZHANG M., PEI W., HUA W., BAO H.: Controlla- 600  
 539 ble highly regular triangulation. *SCIENCE CHINA Information Sciences* 601  
 540 54, 6 (2011), 1172–1183. 2
- 541 [JTPS15] JAKOB W., TARINI M., PANZZO D., SORKINE-HORNUNG 603  
 542 O.: Instant field-aligned meshes. *ACM Trans. on Graphics (Proc. SIG-* 604  
*SIGGRAPH Asia)* 34, 6 (2015), 189:1–189:15. 1, 2, 3, 4, 6, 8, 9, 10
- 544 [LB12] LÉVY B., BONNEEL N.: Variational anisotropic surface meshing 606  
 545 with Voronoi parallel linear enumeration. In *Proceedings of the 21st* 607  
*546 International Meshing Roundtable* (2012), pp. 349–366. 2
- 547 [LJX\*10] LAI Y., JIN M., XIE X., HE Y., PALACIOS J., ZHANG E., 609  
 548 HU S., GU X.: Metric-driven RoSy field design and remeshing. *IEEE Trans.* 610  
*549 on Vis. and Comp. Graphics* 16, 1 (2010), 95–108. 2
- 550 [LL10] LÉVY B., LIU Y.:  $L_p$  centroidal Voronoi tessellation and its ap- 612  
 551 plications. *ACM Trans. on Graphics (Proc. SIGGRAPH)* 29, 4 (2010), 613  
 552 119:1–11. 2, 10
- 553 [LWH\*15] LEUNG Y., WANG X., HE Y., LIU Y., WANG C. C. L.: A 616  
 554 unified framework for isotropic meshing based on narrow-band Eucli- 617  
 555 dean distance transformation. *Computational Visual Media* 1, 3 (2015), 618  
 556 239–251. 2
- 557 [LWL\*09] LIU Y., WANG W., LÉVY B., SUN F., YAN D.-M., LU L., 619  
 558 YANG C.: On centroidal Voronoi tessellation - energy smoothness and 620  
 559 fast computation. *ACM Trans. on Graphics* 28, 4 (2009), 101:1–101:11. 621  
 560 5
- 561 [LWX\*11] LIU Y., XU W., WANG J., ZHU L., GUO B., CHEN F., 623  
 562 WANG G.: General planar quadrilateral mesh design using conjugate 624  
 563 direction field. *ACM Trans. on Graphics (Proc. SIGGRAPH Asia)* 30, 6 (2011), 140:1–140:10. 2
- 564 [LXY\*16] LIU Y.-J., XU C.-X., YI R., FAN D., HE Y.: Manifold dif- 625  
 565 ferential evolution (MDE): A global optimization method for geodesic 566  
 567 centroidal Voronoi tessellations on meshes. *ACM Trans. on Graphics* 626  
*(Proc. SIGGRAPH Asia)* 35, 6 (2016), 243:1–11. 2
- 568 [LZKW10] LI Y., ZHANG E., KOBAYASHI Y., WONKA P.: Editing op- 627  
 569 erations for irregular vertices in triangle meshes. *ACM Trans. on Graphics* 628  
*(Proc. SIGGRAPH Asia)* 29, 6 (2010), 153:1–153:11. 6
- 571 [MKW07] MEYER M., KIRBY R., WHITAKER R.: Topology, accuracy, 629  
 572 and quality of isosurface meshes using dynamic particles. *IEEE Trans.* 630  
*573 on Vis. and Comp. Graphics* 13, 6 (2007), 1704IC1711. 2
- 574 [NPPZ11] NIESER M., PALACIOS J., POLTHIER K., ZHANG E.: Hexa- 632  
 575 gonal global parameterization of arbitrary surfaces. *IEEE Trans. on Vis.* 633  
*576 and Comp. Graphics* 18, 6 (2011), 865–878. 2
- 577 [Ren16] RENKA R. J.: Two simple methods for improving a triangle 635  
 578 mesh surface. *Computer Graphics Forum* 35, 6 (2016), 46–58. 2
- 579 [SAG03] SURAZHSKY V., ALLIEZ P., GOTSMAN C.: Isotropic remes- 637  
 580 hing of surfaces: a local parameterization approach. In *12th Intl. Meshing* 638  
*581 Roundtable* (2003), pp. 204–231. 2
- 582 [SCW\*11] SUN F., CHOI Y.-K., WANG W., YAN D.-M., LIU Y., LÉVY 639  
 583 B.: Obtuse triangle suppression in anisotropic meshes. *Comp. Aided* 640  
*584 Geom. Design* 28, 9 (2011), 537–548. 10
- 585 [SSG03] SIFRI O., SHEFFER A., GOTSMAN C.: Geodesic-based surface 642  
 586 remeshing. In *Proceedings of the 12th International Meshing Roundtable*, 643  
*587 IMR 2003* (2003), pp. 189–199. 2
- 588 [Tur92] TURK G.: Re-tiling polygonal surfaces. In *Proc. ACM SIG-* 645  
*589 GRAPH* (1992), pp. 55–64. 2
- 589 [VCD\*16] VAXMAN A., CAMPEN M., DIAMANTI O., BOMMES D., 647  
 590 HILDEBRANDT K., BEN-CHEN M., PANZZO D.: Directional field 648  
 591 synthesis, design, and processing. In *SIGGRAPH ASIA 2016 Courses* 649  
 (2016), SA ’16, pp. 15:1–15:30. 3
- 592 [VCP08] VALETTE S., CHASSERY J.-M., PROST R.: Generic remes- 651  
 593 hing of 3D triangular meshes with metric-dependent discrete Voronoi 652  
 594 diagrams. *IEEE Trans. on Vis. and Comp. Graphics* 14, 2 (2008), 369– 653  
 595 381. 2
- 596 [WYL\*15] WANG X., YING X., LIU Y.-J., XIN S.-Q., WANG W., GU 656  
 597 X., MUELLER-WITTIG W., HE Y.: Intrinsic computation of centro- 658  
 598 idal Voronoi tessellation (CVT) on meshes. *Computer-Aided Design* 58 659  
 (2015), 51 – 61. 2
- 599 [YBZW14] YAN D.-M., BAO G., ZHANG X., WONKA P.: Low- 660  
 600 resolution remeshing using the localized restricted Voronoi diagram. 661  
*601 IEEE Trans. on Vis. and Comp. Graphics* 20, 10 (2014), 418–1427. 2
- 602 [YLL\*09] YAN D.-M., LÉVY B., LIU Y., SUN F., WANG W.: Isotro- 663  
 603 pic remeshing with fast and exact computation of restricted Voronoi 664  
 604 diagram. *Computer Graphics Forum (Proc. SGP)* 28, 5 (2009), 1445–1454. 665  
 605 1, 2, 3, 5, 6, 8, 9
- 606 [YW13] YAN D.-M., WONKA P.: Gap processing for adaptive maximal 667  
 607 Poisson-disk sampling. *ACM Trans. on Graphics* 32, 5 (2013), 148:1– 668  
 608 148:15. 1, 2, 8, 9
- 609 [YW16] YAN D., WONKA P.: Non-obtuse Remeshing with Centroidal 669  
 610 Voronoi Tessellation. *IEEE Trans. on Vis. and Comp. Graphics* 22, 9 670  
 (2016), 2136–2144. 2
- 611 [ZGW\*13] ZHONG Z., GUO X., WANG W., LÉVY B., SUN F., LIU Y., 672  
 612 MAO W.: Particle-based anisotropic surface meshing. *ACM Trans. on* 673  
*613 Graphics (Proc. SIGGRAPH)* 32, 4 (2013), 99:1–99:14. 2
- 614 [Zha16] ZHANG E.: Course notes rotational symmetries on surfaces: 675  
 615 Theory, algorithms, and applications. In *SIGGRAPH ASIA 2016 Courses* 676  
 (2016), SA ’16, pp. 10:1–10:13. 3

## Appendix: Partial derivatives of field alignment energy

In this appendix, we derive the closed-form partial derivatives of the field alignment energy function, which is required by quasi-Newton optimization methods. Since 2D planar mesh can be re-

garded as a special case of surface mesh, we focus on the field alignment energy of 3D surface mesh.

Given a sample point  $\mathbf{x}_i$  and its neighbor point  $\mathbf{x}_j$ , and the edge  $e$  connecting these two points. The contribution of edge  $e$  to the total field alignment energy comes from its two opposite directions  $e_{ij} = \mathbf{x}_j - \mathbf{x}_i$  and  $e_{ji} = -e_{ij}$ ,

$$\begin{aligned} E_e &= E_{ij} + E_{ji} \\ &= w_{ij} \cdot D_{ij} + w_{ji} \cdot D_{ji} \\ &= w_{ij} \cdot D(e_{ij}, n_i, d_i) + w_{ji} \cdot D(e_{ji}, n_j, d_j), \end{aligned}$$

where  $w_{ij}$  and  $w_{ji}$  are edge weights,  $n_i, n_j, d_i, d_j$  are normal and field vectors at the two points, and  $D$  is the direction distance function.

Viewing the edge weights as a constant, the partial derivative of  $E_e$  with respect to point  $\mathbf{x}_i$  is

$$\frac{\partial E_e}{\partial \mathbf{x}_i} = w_{ij} \frac{\partial D(e_{ij}, n_i, d_i)}{\partial \mathbf{x}_i} + w_{ji} \frac{\partial D(e_{ji}, n_j, d_j)}{\partial \mathbf{x}_i}.$$

The direction distance functions are

$$\begin{aligned} D(e_{ij}, n_i, d_i) &= 1 - \left( \frac{1 + \cos(N\varphi_{ij})}{2} \right) \sin \theta_{ij}, \\ D(e_{ji}, n_j, d_j) &= 1 - \left( \frac{1 + \cos(N\varphi_{ji})}{2} \right) \sin \theta_{ji}, \end{aligned}$$

where  $N$  is the rotation symmetry number of the field,  $(\|e_{ij}\|, \theta_{ij}, \varphi_{ij})$  are the spherical coordinates of  $\mathbf{x}_j$  in local coordinate system at  $\mathbf{x}_i$ , and similarly  $(\|e_{ji}\|, \theta_{ji}, \varphi_{ji})$  are spherical coordinates of  $\mathbf{x}_i$  in local coordinate system at  $\mathbf{x}_j$ . The local coordinate system is illustrated in Fig. 3 (middle).

The partial derivatives are

$$\begin{aligned} \frac{\partial D_{ij}}{\partial \mathbf{x}_i} &= \frac{N \sin(N\varphi_{ij}) \sin \theta_{ij}}{2} \cdot \frac{\partial \varphi_{ij}}{\partial \mathbf{x}_i} - \left( \frac{1 + \cos(N\varphi_{ij})}{2} \right) \cos \theta_{ij} \frac{\partial \theta_{ij}}{\partial \mathbf{x}_i} \\ \frac{\partial D_{ji}}{\partial \mathbf{x}_i} &= \frac{N \sin(N\varphi_{ji}) \sin \theta_{ji}}{2} \cdot \frac{\partial \varphi_{ji}}{\partial \mathbf{x}_i} - \left( \frac{1 + \cos(N\varphi_{ji})}{2} \right) \cos \theta_{ji} \frac{\partial \theta_{ji}}{\partial \mathbf{x}_i}, \end{aligned}$$

$\theta$  and  $\varphi$  are functions of the edge vector  $e$  and local coordinate system  $\{d, n \times d, n\}$ ,

$$\theta = \Theta(e, n, d), \quad \varphi = \Phi(e, n, d).$$

Recall that in spherical coordinate system, the gradient is,

$$\nabla f = \frac{\partial f}{\partial r} \hat{\mathbf{r}} + \frac{1}{r} \frac{\partial f}{\partial \theta} \hat{\theta} + \frac{1}{r \sin \theta} \frac{\partial f}{\partial \varphi} \hat{\varphi},$$

where  $\hat{\mathbf{r}}, \hat{\theta}, \hat{\varphi}$  are the local orthogonal unit vectors in the direction of increasing  $r, \theta$  and  $\varphi$ .

so,

$$\nabla \theta = \frac{1}{r} \hat{\theta}, \quad \nabla \varphi = \frac{1}{r \sin \theta} \hat{\varphi}.$$

$$\begin{aligned} \frac{\partial \Theta}{\partial e} &= \frac{1}{\|e\|} \hat{\theta} \\ &= \frac{e \times (e \times n)}{\|e\|^2 \|e \times n\|} \\ \frac{\partial \Phi}{\partial e} &= \frac{1}{\|e\| \sin \theta} \hat{\varphi} \\ &= \frac{\hat{\mathbf{r}} \times \hat{\theta}}{\|e \times n\|} \\ &= \frac{1}{\|e \times n\|} e \times \frac{\partial \Theta}{\partial e} \\ &= -\frac{e \times n}{\|e \times n\|^2}. \end{aligned}$$

In the case of  $\mathbf{x}_i$  and  $\mathbf{x}_j$ ,

$$\begin{aligned} \theta_{ij} &= \Theta(e_{ij}, n_i, d_i) \\ \varphi_{ij} &= \Phi(e_{ij}, n_i, d_i) \\ \theta_{ji} &= \Theta(e_{ji}, n_j, d_j) \\ \varphi_{ji} &= \Phi(e_{ji}, n_j, d_j). \end{aligned}$$

The partial derivatives with respect to  $\mathbf{x}_i$  are

$$\begin{aligned} \frac{\partial \theta_{ij}}{\partial \mathbf{x}_i} &= \frac{\partial \Theta}{\partial e_{ij}} \frac{\partial e_{ij}}{\partial \mathbf{x}_i} + \frac{\partial \Theta}{\partial n_i} \frac{\partial n_i}{\partial \mathbf{x}_i} + \frac{\partial \Theta}{\partial d_i} \frac{\partial d_i}{\partial \mathbf{x}_i} \\ &= -\frac{\partial \Theta}{\partial e_{ij}} + \frac{\partial \Theta}{\partial n_i} \frac{\partial n_i}{\partial \mathbf{x}_i} + \frac{\partial \Theta}{\partial d_i} \frac{\partial d_i}{\partial \mathbf{x}_i}, \end{aligned}$$

$$\begin{aligned} \frac{\partial \varphi_{ij}}{\partial \mathbf{x}_i} &= \frac{\partial \Phi}{\partial e_{ij}} \frac{\partial e_{ij}}{\partial \mathbf{x}_i} + \frac{\partial \Phi}{\partial n_i} \frac{\partial n_i}{\partial \mathbf{x}_i} + \frac{\partial \Phi}{\partial d_i} \frac{\partial d_i}{\partial \mathbf{x}_i} \\ &= -\frac{\partial \Phi}{\partial e_{ij}} + \frac{\partial \Phi}{\partial n_i} \frac{\partial n_i}{\partial \mathbf{x}_i} + \frac{\partial \Phi}{\partial d_i} \frac{\partial d_i}{\partial \mathbf{x}_i}, \end{aligned}$$

$$\begin{aligned} \frac{\partial \theta_{ji}}{\partial \mathbf{x}_i} &= \frac{\partial \Theta}{\partial e_{ji}} \frac{\partial e_{ji}}{\partial \mathbf{x}_i} + \frac{\partial \Theta}{\partial n_j} \frac{\partial n_j}{\partial \mathbf{x}_i} + \frac{\partial \Theta}{\partial d_j} \frac{\partial d_j}{\partial \mathbf{x}_i} \\ &= \frac{\partial \Theta}{\partial e_{ji}}, \end{aligned}$$

$$\begin{aligned} \frac{\partial \varphi_{ji}}{\partial \mathbf{x}_i} &= \frac{\partial \Phi}{\partial e_{ji}} \frac{\partial e_{ji}}{\partial \mathbf{x}_i} + \frac{\partial \Phi}{\partial n_j} \frac{\partial n_j}{\partial \mathbf{x}_i} + \frac{\partial \Phi}{\partial d_j} \frac{\partial d_j}{\partial \mathbf{x}_i} \\ &= \frac{\partial \Phi}{\partial e_{ji}}. \end{aligned}$$

We assume that the local variance of the normal and field direction is small, thus

$$\frac{\partial n_i}{\partial \mathbf{x}_i} \approx 0, \quad \frac{\partial d_i}{\partial \mathbf{x}_i} \approx 0.$$

650 In this condition, we get

$$\begin{aligned}\frac{\partial \theta_{ij}}{\partial \mathbf{x}_i} &\approx -\frac{\partial \Theta(e_{ij}, n_i, d_i)}{\partial e_{ij}} = -\frac{e_{ij} \times (e_{ij} \times n_i)}{\|e_{ij}\|^2 \|e_{ij} \times n_i\|} \\ \frac{\partial \varphi_{ij}}{\partial \mathbf{x}_i} &\approx -\frac{\partial \Phi(e_{ij}, n_i, d_i)}{\partial e_{ij}} = \frac{e_{ij} \times n_i}{\|e_{ij} \times n_i\|^2} \\ \frac{\partial \theta_{ji}}{\partial \mathbf{x}_i} &= \frac{\partial \Theta(e_{ji}, n_j, d_j)}{\partial e_{ji}} = \frac{e_{ij} \times (e_{ij} \times n_j)}{\|e_{ij}\|^2 \|e_{ij} \times n_j\|} \\ \frac{\partial \varphi_{ji}}{\partial \mathbf{x}_i} &= \frac{\partial \Phi(e_{ji}, n_j, d_j)}{\partial e_{ji}} = \frac{e_{ij} \times n_j}{\|e_{ij} \times n_j\|^2}.\end{aligned}$$

The total partial derivative of  $E_{\text{field}}$  with respect to point  $\mathbf{x}_i$  is

$$\frac{\partial E_{\text{field}}}{\partial \mathbf{x}_i} = \sum_{j \in \mathcal{N}(i)} \left( w_{ij} \cdot \frac{\partial D_{ij}}{\partial \mathbf{x}_i} + w_{ji} \cdot \frac{\partial D_{ji}}{\partial \mathbf{x}_i} \right).$$